Open Ceramics 11 (2022) 100292

Contents lists available at ScienceDirect

Open Ceramics

journal homepage: www.sciencedirect.com/journal/open-ceramics

# Stable, asymmetric, tubular oxygen transport membranes of $(Sc_2O_3)_{0.10}(Y_2O_3)_{0.01}(ZrO_2)_{0.89}$ – $LaCr_{0.85}Cu_{0.10}Ni_{0.05}O_{3-\delta}$

Lev Martinez Aguilera [a], Stéven Pirou [a], Peyman Khajavi [a], Julio García-Fayos [b], Jose Manuel Serra [b], Henrik Lund Frandsen [a], Peter Vang Hendriksen [a], Andreas Kaiser [a], Ragnar Kiebach [a], Astri Bjørnetun Haugen [a,*]

[a] Department of Energy Conversion and Storage, Technical University of Denmark, Anker Engelunds Vej 1, 2800 Kgs, Lyngby, Denmark
[b] Instituto de Tecnología Química (Universitat Politècnica de Valencia – Consejo Superior de Investigaciones Científicas), Av. Los Naranjos S/n, E-46022 Valencia, Spain

A B S T R A C T

Oxygen transport membranes have the potential to deliver pure and cheap oxygen to chemical reactors, combustors, gasifiers etc., given that geometry, microstructure and material properties are optimized. This work demonstrates the first successful preparation of dual-phase tubular, asymmetric oxygen transport membranes consisting of a new electronic conductor $LaCr_{0.85}Cu_{0.10}Ni_{0.05}O_{3-\delta}$ mixed with $(Sc_2O_3)_{0.10}(Y_2O_3)_{0.01}(ZrO_2)_{0.89}$ as ionic conductor. Challenges related to Cr-volatility were overcome by using $Fe_2O_3$ as a sintering aid. The sintering aid decreased mismatches in shrinkage and thermal expansion between the four layers in the asymmetric membrane and decreased the sintering temperature such that the Cr-volatility was suppressed. The membranes reached an oxygen flux of 0.28 $ml \bullet min^{-1} \bullet cm^{-2}$ in an air/$N_2$ atmosphere at 950 °C. Furthermore, the membranes showed a stable oxygen flux after exposure to different atmospheres, including air/$CO_2$ and air/$H_2$ gradients. The successful fabrication of stable, asymmetric, tubular membranes opens the possibility for future integration in syngas or oxy-combustion applications.

## 1. Introduction

Oxygen is an important commodity worldwide with several industrial applications and a growing market [1,2], being the third largest volume chemical with a yearly production of ca. 100 Mton [3]. Currently, industrial production of oxygen is dominated by two technologies: 1) fractional distillation of liquefied air, a large-scale production technology generating high purity oxygen (>99%), and 2) pressure swing adsorption (PSA), that uses pressurized systems and absorbents like carbon molecular sieves or zeolites to remove $N_2$ and $CO_2$ from the air. However, oxygen produced by PSA is only <97% pure, and the investment cost and process scale for distillation of liquefied air are massive [1,4].

Oxygen transport membranes (OTMs) are a promising alternative for high-temperature separation of oxygen from air [5,6]. An OTM is a gas-tight ceramic layer only permeable to oxygen ions and electrons, allowing a theoretical oxygen selectivity of 100%. The total oxygen flux depends on the ionic and electronic conductivity, membrane thickness, splitting and recombination rates of molecular oxygen at the membrane/gas interfaces and gas permeability of the support layer. A difference in partial oxygen pressure ($pO_2$) between the feed and the permeate side of the membrane provides the driving force for the process [7,8].

Promising applications for OTMs are oxy-fuel combustion where downstream $CO_2$ capture is targeted and oxygen blown gasification. When air is used in combustion processes, extra energy is needed to heat the inactive $N_2$ gas, i.e. ~79% of the air's volume, which lowers the efficiency. It also increase the capital costs of the combustion equipment, since dimensioning to handle the inactive $N_2$ is needed [1,9,10]. Moreover, downstream $CO_2$ capture form an exhaust stream is much simpler and cheaper if it does not require a $CO_2/N_2$ separation as is the case when air is used in the combustion. Biomass gasification is an especially interesting application [9,11]. However, in order to use OTMs in a tubular geometry suitable for integration for larger scale and real operation conditions, technical challenges related to the stability and the performance of the membrane materials under operating conditions of biomass gasification (ca 850 °C - 1000 °C and $pO_2$ of $10^{-20}$ atm) need to be addressed [7].

Mixed ionic-electronic conducting perovskite structures with the composition $A_xSr_{1-x}Co_yFe_{1-y}O_{3-d}$ (A = La, Ba) have high oxygen-ionic and electronic conductivity, which are the basic requirements for an OTM material. However, these perovskites have a limited $pO_2$ operation range and can decompose at low $pO_2$ values (~$10^{-12}$ atm) [12] and are also affected by carbonation when exposed to $CO_2$-containing

* Corresponding author.
*E-mail address:* ahua@dtu.dk (A.B. Haugen).

https://doi.org/10.1016/j.oceram.2022.100292
Received 31 March 2022; Received in revised form 2 June 2022; Accepted 5 July 2022
Available online 8 July 2022

environments [13–15]. By using dual-phase composites, with one electronic and one ionic conducting phase, it is possible to optimize either material in terms of stability and performance [16]. Fluorite-structured oxides based on $Y_2O_3$-stabilized $ZrO_2$ (YSZ) have been widely studied as ionic conductors due to their highly stable conductivity in the $pO_2$ range between 1 and $10^{-21}$ [17,18]. By co-doping YSZ with Sc, as in $(Sc_2O_3)_{0.10}(Y_2O_3)_{0.01}(ZrO_2)_{0.89}$ – ScYSZ, an ionic conductivity up to 0.12 S $cm^{-1}$ at 850 °C can be obtained [19,20].

Lanthanum chromite-based perovskites $La_{1-x}A_xB_yCr_{1-y}O_{3-\delta}$ (A = Sr, Ca; B = Fe, Cu, Mn, Co) have been studied as solid oxide cell interconnects due to their high thermo-chemical stability at high temperatures (~1000 °C), excellent stability in reducing environments ($pO_2$ ~$10^{-20}$ atm) [21,22], and decent electronic conductivity. Ca or Sr-doped lanthanum chromite have an electronic conductivity that can reach up to 25 S $cm^{-1}$ and 6 S $cm^{-1}$ at 1000 °C in air and reducing conditions, respectively [21,23–26]. In addition, doping with Sr can accelerate the oxygen exchange kinetics [27]. However, in $pO_2 < 10^{-7}$ and above 600 °C, Sr segregates and the electronic conductivity decreases exponentially [24,26,27]. Thus, a Sr-free chromite is advantageous for highly reducing environments and temperatures as high as 1000 °C; operation conditions foreseen for OTMs in gasification processes.

Previously, Pirou et al. [28] demonstrated that $LaCr_{0.85}Cu_{0.10}Ni_{0.05}O_{3-\delta}$ – LCCN – and ScYSZ can be combined to form an electronic and ionic conducting dual-phase OTM for oxy-fuel applications. However, manufacturing such chromite-based, asymmetric dual-phase materials with a thin (~10 μm), dense active membrane on a thick (~700 μm) porous support, was not successful [29], due to the following challenges: 1) formation of transversal cracks in the membrane, caused by sintering stress or thermal expansion mismatches, 2) formation of longitudinal cracks caused by vaporization of Cr from LCCN and subsequent hydration of $La_2O_3$ to La $(OH)_3$, and 3) segregation of an insulating secondary phase, $LaZr_2O_7$, on the membrane surface [29]. The two latter problems are directly related to the high volatility of Cr [30] and its evaporation from LCCN [29] at the high sintering temperature needed to densify the LCCN (1450 °C). Avoiding the evaporation of Cr is therefore a cornerstone to keep the integrity of the LCCN phase and manufacture OTMs with a stable performance in reducing conditions. At the same time, the sintering stresses and thermal expansion of all the layers of the asymmetric membrane must be carefully tailored.

Using sintering aids in the active membrane may allow densification of the membrane layer at lower sintering temperatures [31]. If a sintering aid is added to the porous support, increased support shrinkage can potentially place the active membrane layer under compressive stress. This can aid the densification of the membrane [32], as long as it has reached a temperature where its sintering has been activated. Additionally, sintering aids may reduce mismatches in thermal expansion coefficient (TEC) between the various membrane components and layers, minimizing stresses during thermal cycling.

This work describes investigations to use $Fe_2O_3$ as a sintering aid with the aim to tailor the thermo-mechanical properties of the components (both between the membrane layers and between the individual phases in each layer) in the asymmetrical ScYSZ-LCCN OTMs on 3 mol% $Y_2O_3$-stabilized $ZrO_2$ (3YSZ) tubular porous supports. $Fe_2O_3$ was chosen as the sintering aid for the materials in this work based on previous reports on sintering aids in YSZ [33,34]. With this approach, Cr vaporization could be avoided and the sintering temperature reduced to 1250 °C, resulting in dense and robust LCCN-ScYSZ membrane layers in an asymmetric OTM architecture.

## 2. Experimental

The asymmetric tubular oxygen transport membrane (OTM) architecture consist of four layers (a porous support, an inner porous activation layer, a dense active membrane, and an outer porous activation layer), as shown in Fig. 1.

### 2.1. Powder pre-treatment

Powders of $(Sc_2O_3)_{0.10}(Y_2O_3)_{0.01}(ZrO_2)_{0.89}$ – ScYSZ (Daiichi, Japan) and $LaCr_{0.85}Cu_{0.10}Ni_{0.05}O_{3-\delta}$ – LCCN (CerPoTech, Norway) were mixed in different volumetric proportions to prepare the different dual-phase composites investigated in this work. $Fe_2O_3$ (Alfa Aesar, USA) was added in 1 and 3 mol% to adjust the sintering behaviour of the different composites. Samples of single-phase ScYSZ and 3YSZ powders were also prepared. The powders were mixed by ball milling in ethanol using 5 mm $ZrO_2$ milling media until the mean particle size was below 250 nm.

### 2.2. Preparation of tubular, asymmetric oxygen transport membranes

The fabrication process of the dual-phase membranes is summarised in Fig. 2. Tubular porous supports were prepared by thermoplastic extrusion process following the previously developed procedure [29,35,36]. A volumetric-based mixture of graphite (Superior Graphite, USA), poly-methyl-methacrylate (Esprix, USA) ethylene-vinyl acetate copolymer (DuPont, USA) and paraffin wax (Sigma-Aldrich, USA) was added to 3YSZ powders (Tosoh, Japan) coated with stearic acid (Sigma-Aldrich, USA). Three different feedstocks were prepared, with 0, 1 or 3 mol % $Fe_2O_3$. The feedstocks were mixed and homogenized for 2 h at 100 °C using a BK20 mixer (Linden International, Germany). Tubes of 14 mm outer diameter and 1 mm wall thickness were extruded at 85 °C using a single screw extruder 19/20DN (Brabender, Germany).

Dip coating slurries for the active membrane and activation layers were made according to the formulation proportions described in Table S1 (supplementary information). Ethanol was used as solvent, polyvinyl-pyrrolidone (PVP) K15 (Sigma-Aldrich, USA) as dispersant, PVP K30 (Sigma-Aldrich, USA) and polyvinyl-butyral (PVB) Mowital B30HH (Kuraray, USA) as binders, dibutyl sebacate (DBS) (Sigma Aldrich, USA) as plasticizer and graphite UF-1 (Graphit Kropfmühl, Germany) as pore former. The oxide powders, dispersant and solvent were ball milled for 72 h. Afterwards, the binder and plasticizer were added and subsequently ball-milled for 2 h, filtered through a 20 μm mesh filter paper and stored at constant rotation (5 rpm) to avoid agglomeration. Deposition on the tubular supports was done with an in-house built dip coater [37] varying the deposition speeds from 0.05 to 0.5 cm•$s^{-1}$ to obtain 4–10 μm thick layers.

A ramp of 15 °C•$h^{-1}$ and dwells of 2 h at 200 °C, 360 °C and 600 °C were used for the binder burnout of the porous support and the calcination of the inner layer. A maximum temperature of 950 °C was reached and kept for 2 h to finalize the calcination. After that the furnace was cooled down at a rate of 120 °C•$h^{-1}$. This cooling rate was used for all thermal treatments in this work. The active membrane was deposited on the calcined inner layer. The dip-coating speed was adjusted to obtain uniform layers of 5–8 μm thickness. The membrane was sintered by first heating at a ramp of 60 °C•$h^{-1}$ with dwells at 360 °C and 600 °C for 2 h each. Two different ramp rates (60 and 200 °C•$h^{-1}$) were used from 600 °C up to the sintering temperature (1250 °C, held for 4 h). The outer activation layer was deposited on the sintered active membrane layer followed by a final thermal program with the same debinding step as for the membrane sintering, followed by heating at 200 °C•$h^{-1}$ from 600 °C to 1200 °C and a 2 h dwell.

### 2.3. Characterization

The particle size of the slurries was measured with a laser diffraction particle size analyser LS 13 320 (Beckman Coulter, USA). Rheological properties of the slurries were analyzed using a MCR302 rheometer (Anton Paar, Austria) with a 25 mm stainless steel parallel plate (PP25) at a gap of 0.5 mm. Sintering curves and thermal expansion coefficients (TEC) were obtained from 10 mm long rods on a DIL402CD dilatometer (Netzsch, Germany). For the sintering curves, pellets of uniaxially

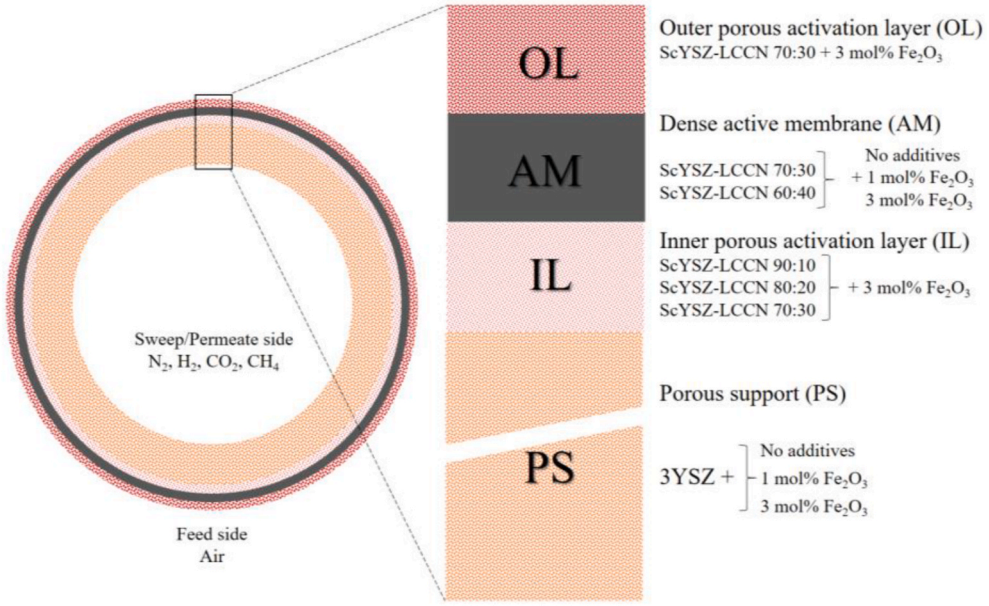


**Fig. 1.** Schematic of the oxygen transport membrane architecture and materials analyzed in this study.

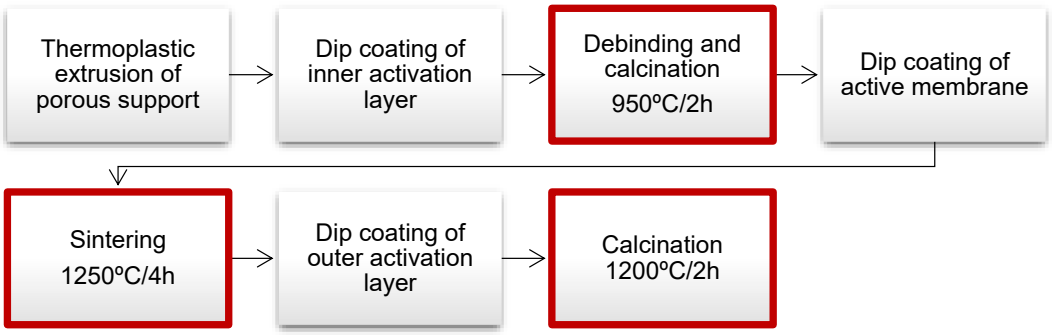


**Fig. 2.** Manufacturing steps of the asymmetric tubular oxygen transport membranes. Thermal processes are outlined in red. (For interpretation of the references to colour in this figure legend, the reader is referred to the Web version of this article.)

pressed powders were heated with a rate of 1 °C•min$^{-1}$ up to 1250 °C and cooled using a ramp of 10 °C•min$^{-1}$. Pellets for the TEC measurements were pre-sintered in a chamber furnace in stagnant air at 1350 °C for 2 h. The TEC measurements were performed using heating and cooling ramps of 2 °C•min$^{-1}$ with 1 h dwell at 1250 °C, with a 6 mm alumina rod as a reference.

The strength of the porous supports was measured by four-point bending at room temperature. A maximum load of 10 N was applied. The test specimens were 6 cm long and semi-cylindrical, obtained by cutting the sintered tubes in two along their length direction. At least six specimens of each porous support were tested to obtain representative data. The test rig, loading fixture and methodology are described in more details by Kwok et al. [38]. The Darcy gas permeability constant of the porous supports was calculated by measuring the flow rate of $N_2$ through the supports at known pressure gradients at room temperature. The setup is described in more details in Ref. [39]. The porosity of the porous support was characterized by Hg-intrusion using a PoreMaster 33 (Quantachrome, USA) and microstructure analysis using the scanning electron microscopes (SEM) TM3000 (Hitachi, Japan) or Merlin (Zeiss, Germany) with energy-dispersive spectroscopy (EDS) (XFlash 6–60, Bruker, USA). Image J (open source software) was used for the SEM data analysis.

Oxygen permeability through the asymmetric, tubular membrane was tested by supplying air at the feed side (outer side) and various sweep gasses at the permeate side (inner side) as shown in Fig. 1. More details of the setup can be found in the supplementary information, Section S.2. Cyclic cooling and heating was applied to investigate the mechanical and chemical stability of the membranes: heating up to 1000 °C with a ramp rate of 2 °C•min$^{-1}$, 30 min dwell and then cooling down with the same rate. This cycle was repeated 4 times in air and 3 times in 5%$H_2$–$N_2$. A final cycle in air was carried out to re-oxidise the sample.

### 2.4. Sample codes

The amount of ScYSZ, LCCN and $Fe_2O_3$ of the different layers is abbreviated as "SL*x*y*F*z", where S is for ScYSZ and *x* its content in vol%; L is for LCCN and *y* its content in vol%; and F for $Fe_2O_3$ and *z* its mol% added. For example, SL9010Fe3 refers to 90 vol% ScYSZ, 10 vol% LCCN with an addition of 3 mol% $Fe_2O_3$.

## 3. Results and discussion

### 3.1. Effect of $Fe_2O_3$ doping

#### 3.1.1. Thermomechanical properties of the OTM materials

We used dilatometry to assess the effect of $Fe_2O_3$ doping on the membrane components' thermomechanical properties (sintering

behaviour and TEC). Fig. 3 shows the shrinkage of cylindrical pellets made Fe-doped materials (used for the porous support and active membrane) during sintering. The temperature for the onset of sintering and the TEC are listed in Table 1 (with a split into four different temperature intervals to account for the temperature dependence of the TEC values).

Fig. 3a shows the sintering curves of the material for the porous support, 3YSZ, with different amount of $Fe_2O_3$ doping. A decrease of 67 °C in the sintering onset temperature was observed by adding 1 mol% $Fe_2O_3$ (3YSZFe1). Further increase of the $Fe_2O_3$ content has a lower effect on the sintering; only a decrease by 10 °C was observed between the samples with 1 mol% (3YSZFe1) and 3 mol% (3YSZFe3) $Fe_2O_3$ doping. The sintering rates were not affected by the addition of $Fe_2O_3$. The total shrinkage reached at 1250 °C increases with the same trend, from 10% in undoped 3YSZ to 18% in 3YSZFe1 and 20% in 3YSZFe3. These results are is in good agreement with literature: doping 8YSZ with 3 mol% Fe was found to have no considerable effect on the sintering rate, but lowered the onset of sintering by approximately 100 °C [33,34]. This is caused by the co-existence of substitutional and interstitial $Fe^{3+}$ ions that increase the $Zr^{4+}$ diffusion coefficient [34]. Fig. 3b shows the effect of $Fe_2O_3$ doping on sintering of the active membrane material SL7030 (70 vol% ScYSZ, 30 vol% LCCN). As seen, the onset temperatures for sintering increased with the addition of dopant, but the total shrinkage reached at 1250 °C still increases, from 6% in SL7030 to 7% in SL7030Fe1 (SL7030 with 1 mol% $Fe_2O_3$) and 11% in SL7030Fe3 (SL7030 with 3 mol% $Fe_2O_3$).

Doping with $Fe_2O_3$ also affects the thermal expansion coefficient (TEC) of both the porous support and active membrane materials, as seen in Table 1. The TEC of the single components (3YSZ, ScYSZ and LCCN) presented in Table 1 are in accordance with literature [40–42]. TEC values of the support material, 3YSZ, decrease with increasing Fe content below 650 °C; a difference of $2 \times 10^{-6}$ $K^{-1}$ between pure 3YSZ and 3YSZFe3 was found in the interval 50–650 °C. However, the effect is inverted at higher temperatures; the TEC of 3YSZFe3 is $0.71 \times 10^{-6}$ $K^{-1}$ higher than of 3YSZ in the range 1050–1250 °C. The TEC of the active membrane materials decrease with increasing Fe content over the entire studied temperature range, but most markedly at higher temperatures.

### 3.1.2. Properties of the tubular supports

Since the asymmetric membranes rely on the mechanical and physical properties of the porous support, these properties were investigated before fabrication of multi-layered OTM was attempted. Porous tubular supports of 3YSZ with 0, 1 and 3 mol% $Fe_2O_3$ were fabricated and their main properties after sintering are displayed in Table 2.

Fig. 4 shows cross-sectional SEM micrographs of the sintered tubes. Long, irregular pores are formed by graphite, while PMMA provides the larger spherical pores. The pores from PMMA are observed in all the samples, while the pores from graphite (Fig. 4a) are partially collapsed in 3YSZFe1 (Fig. 4b) and 3YSZFe3 (Fig. 4c). The total porosity generally decreases with $Fe_2O_3$ doping, but the pore size increases slightly.

The gas permeability of the supports, expressed with the Darcy permeability coefficients (Table 2), are unaffected by the doping. This can be explained by how the doping influences the sintering and more directly the microstructure, analogous to observations in the same material system when increasing the sintering temperature [43]. The increased densification, either by doping or higher sintering temperature, causes higher shrinkage (as observed by dilatometry, Fig. 3a) and lower total pore volume measured by mercury porosimetry (Table 2). At the same time, the remaining pores are brought in closed contact and coarsen (through an Ostwald ripening effect [43]), such that the remaining pore channels between them are wider. The effective pore size, as measured by mercury porosimetry (Table 2), therefore increases. These two microstructural changes affect the permeability in opposite directions, such that the effect of reduced porosity volume is compensated by larger pore channels. This is also in accordance with previous studies [39,44]. All the three porous supports fulfil the requirement of a gas permeability larger than $1 \times 10^{-14}$ $m^{-2}$, for which gas permeability limitations through the support are not expected [39].

The strength values (Table 2) increase with the dopant content. By using 1 mol% $Fe_2O_3$, the strength of the 3YSZ porous support increases by 38%. In the case of 3YSZFe3, a strength of >138 MPa was calculated (the samples could withstand the maximum testing load of the equipment (10 N)). The increased strength is an expected result of the improved densification of the $Fe_2O_3$-doped porous support.

### 3.2. Analysis of porous support – active membrane material combinations

Having established the thermomechanical properties of our active membrane and porous support materials with $Fe_2O_3$ doping (Table 1), we can now proceed to identify material combinations with similar thermal properties suitable for co-sintering. Fig. 5 is a graphic representation of the TEC and TEC mismatch of all combinations of the three 3YSZ-based porous support and three ScYSZ-LCCN-based active membranes. The figure shows that the combinations with lower TEC mismatches (below $10^{-6}$ $K^{-1}$ in all temperature ranges) are (i) 3YSZFe1 - SL7030Fe1, (ii) 3YSZFe1 - SL7030Fe3 and (iii) 3YSZFe3 - SL7030Fe3. A similar analysis was made using Fe-doped SL6040 (60% ScYSZ, 40% LCCN) composites for the active membrane material. These composites have higher content of LCCN to ensure percolation of the electronic-conductor phase within the membrane. 3YSZFe3 - SL6040Fe3 was found to be a suitable combination.

The differences in the onset temperature for sintering of porous support and active membrane combinations are shown in Table 3. While this difference is more than 100 °C for the undoped samples, it decreases by $Fe_2O_3$ doping in both the porous support and the membrane materials, down to practically zero difference between SL7030Fe3 and

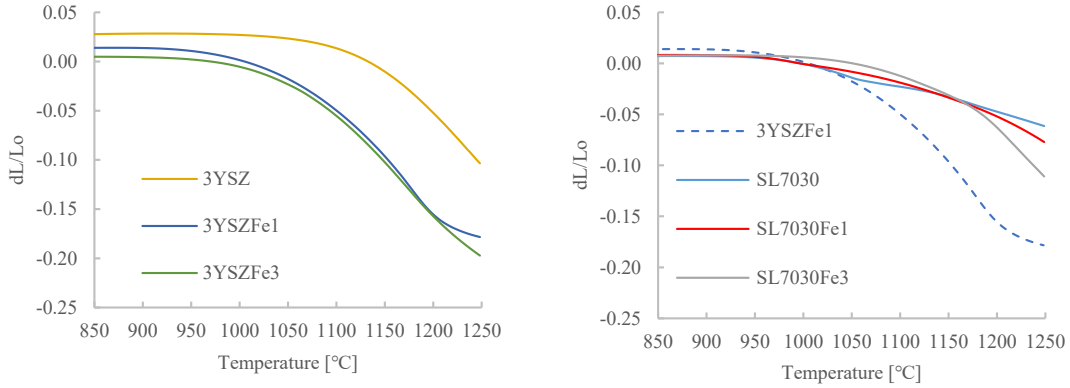


**Fig. 3.** a) Sintering curves of porous support materials. 3YSZ, 3YSZFe1 (YSZ with 1 mol% $Fe_2O_3$) and 3YSZFe3 (YSZ with 3 mol% $Fe_2O_3$), b) Sintering curves of Fe-doped 3YSZ and Fe-doped active membrane composite materials.

**Table 1**
Thermal expansion coefficients (TECs) and sintering onset temperatures of membrane components. The TEC is reported for four different temperature intervals due to its temperature dependence.

| Material | 50–650 °C | 650–850 °C | 850–1050 °C | 1050–1250 °C | Sintering onset [°C] |
|---|---|---|---|---|---|
| ScYSZ | 10.1 | 12.1 | 13.1 | 13.8 | 987 |
| LCCN | 9.5 | 10.8 | 11.7 | 12.2 | 993 |
| 3YSZ | 10.4 | 10.7 | 11.6 | 12.9 | 1103 |
| 3YSZFe1 | 9.7 | 10.5 | 12.3 | 13.0 | 1036 |
| 3YSZFe3 | 8.4 | 11.1 | 11.9 | 13.6 | 1025 |
| SL7030 | 9.4 | 11.4 | 12.9 | 13.7 | 977 |
| SL7030Fe1 | 9.4 | 11.2 | 12.6 | 13.5 | 997 |
| SL7030Fe3 | 9.1 | 11.1 | 12.4 | 13.1 | 1035 |
| SL6040 | 8.9 | 11.0 | 12.6 | 13.2 | 963 |
| SL6040Fe3 | 8.5 | 11.2 | 12.5 | 13.4 | — |
| SL8020 | 9.5 | 11.6 | 12.9 | 13.5 | 947 |
| SL9010 | 9.0 | 11.7 | 12.7 | 13.2 | — |
| SL9010Fe3 | 8.6 | 11.1 | 12.5 | 13.1 | 1036 |

**Table 2**
Main features of the $Fe_2O_3$-doped 3YSZ porous supports.

| Sample | 3YSZ (0 mol% $Fe_2O_3$) | 3YSZFe1 (1 mol% $Fe_2O_3$) | 3YSZFe3 (3 mol% $Fe_2O_3$) |
|---|---|---|---|
| Porosity [vol%] | 59.9 | 53.4 | 48.6 |
| Pore size [μm] | 1.29 | 1.37 | 1.38 |
| Darcy coefficient [$10^{-14}$ $m^{-2}$] | 2.2 | 2.1 | 2.2 |
| Average strength [MPa] | 83 ± 4 | 114 ± 3 | >138 |
| Sintering onset temperature [°C] | 1110 | 1040 | 1037 |
| Diameter shrinkage [%] | 19.9 | 24.9 | 25.7 |

3YSZFe1.

### 3.3. Fabrication of asymmetrical tubular oxygen membranes

The most promising combinations of materials for porous support/active membrane, presented in the analysis above, were prepared as tubular, multi-layered asymmetric membranes. The interactions between them, as well as the inner and outer activation layers, are described in the following sections.

#### 3.3.1. Effect of the porous support on the dense active membrane

3YSZ porous supports containing 0, 1 and 3 mol% $Fe_2O_3$ were prepared to be able to later assess the influence of the porous support on the densification of the active membrane. The SEM images of the sintered cross-section of these supports in combination with a SL6040Fe3 active membrane and a SL9010Fe3 inner activation layer are shown in Fig. 6. The active membrane layer densifies more with increasing content of $Fe_2O_3$ in the YSZ support.

Some proposed porous support/active membrane combinations described in Section 3.2 considered the use of 3YSZFe1 porous support. However, the membrane layer did not densify in any of the prepared systems with 3YSZ or 3YSZFe1 porous support, irrespective of the Fe-content in the ScYSZ-LCCN active membrane. In contrast, all the active membranes co-sintered with 3YSZFe3 porous support showed >90% densification. The improved densification of the active membrane with increasing $Fe_2O_3$ content in the porous support can be ascribed to the increased total shrinkage of the porous support (Table 2 and Fig. 2), which is the structurally dominating part of the component. This generates compressive stresses in the membrane layer that likely assist its densification as long as the two materials shrink at similar temperatures.

#### 3.3.2. Effect of Fe-content in the dense active membrane

In order to analyse the effect of the $Fe_2O_3$-content in the active membrane on its densification, SL7030, SL7030Fe1 and SL7030Fe3 active membrane layers were deposited on tubes of the 3YSZFe3 porous support with SL9010Fe3 as the inner activation layer. All the active membrane layers densified, regardless the quantity of $Fe_2O_3$ in the active membrane's formulation.

Since evaporation from $Fe_2O_3$ starts around 1050 °C [45], it is likely that a significant amount vaporizes and redistributes during the sintering process at 1250 °C, for example from the 3YSZFe3 porous support or the SL9010Fe3 inner activation layer and into the active membrane. The elemental composition from EDS of the SL7030, SL7030Fe1 and SL7030Fe3 active membrane when deposited on SL9010Fe3 inner activation layer and supported on 3YSZFe3 porous support is shown in Table 4. This confirms that Fe has propagated into the SL7030 membrane layer. Fe seems to have a preference for the LCCN phase, but because of the small average grain size of the LCCN (~330 nm) and of the ScYSZ (~900 nm) in the active membrane, the EDS could include signals from both phases.

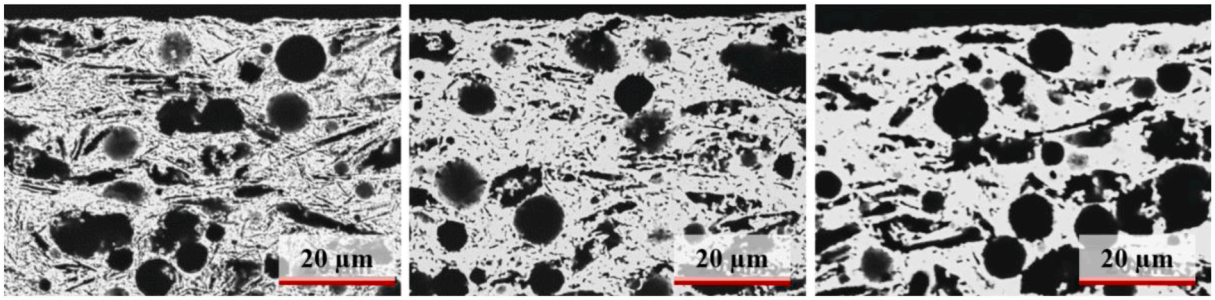


**Fig. 4.** Cross-sectional SEM micrographs of $Fe_2O_3$-doped 3YSZ tubular supports after sintering at 1250 °C for 4 h. (a) Single phase 3YSZ, (b) 1 mol% doped $Fe_2O_3$ and (c) 3 mol% doped $Fe_2O_3$.

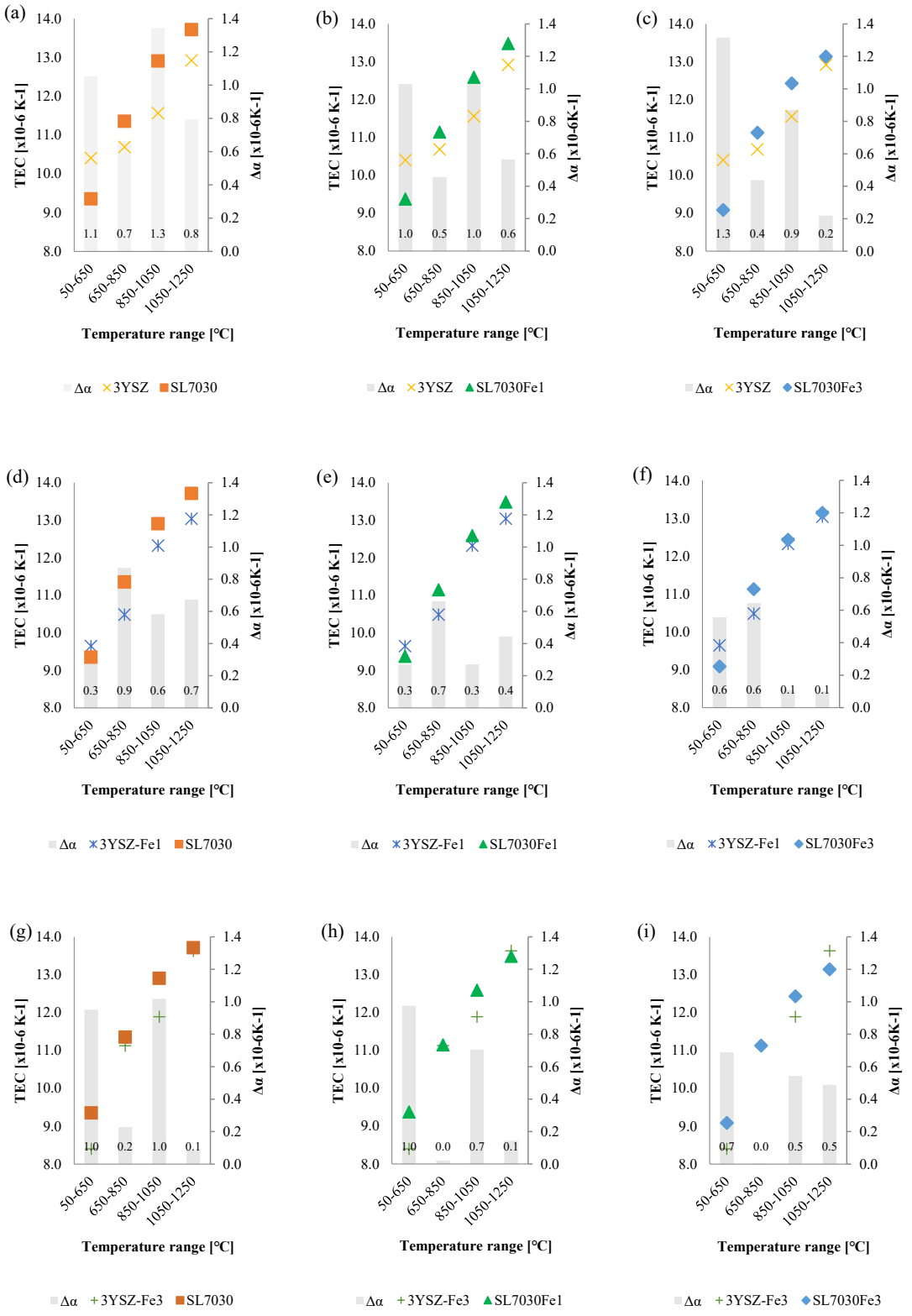


**Fig. 5.** TEC analyses of 3YSZ-based porous supports and ScYSZ-LCCN active membrane materials with differents $Fe_2O_3$ concentrations as sintering aid.

### 3.3.3. *Active membrane – porous support interaction at different heating rates*

The interaction between the 3YSZFe3 porous support and the SL7030Fe3 active membrane layer was studied with two different heating rates (60 or 200 °C $h^{-1}$) between 600 °C and 1250 °C, to analyse the possible effects caused by the different shrinkage behaviour of the materials. SEM analysis of the active membrane's surface revealed extensive cracks on the set of samples sintered with ramp of 60 °C $h^{-1}$ (Fig. 7a); however, when using a heating rate of 200 °C $h^{-1}$, crack-free membranes were obtained (Fig. 7b). Additionally, a higher membrane

**Table 3**
Difference in sintering onset temperature (°C) between materials used in the active membrane (vertical) and in the porous support (horizontal).

| Materials | 3YSZ | 3YSZFe1 | 3YSZFe3 |
|---|---|---|---|
| SL7030 | 126 | 59 | 48 |
| SL7030Fe1 | 106 | 40 | 28 |
| SL7030Fe3 | 68 | 1 | 10 |

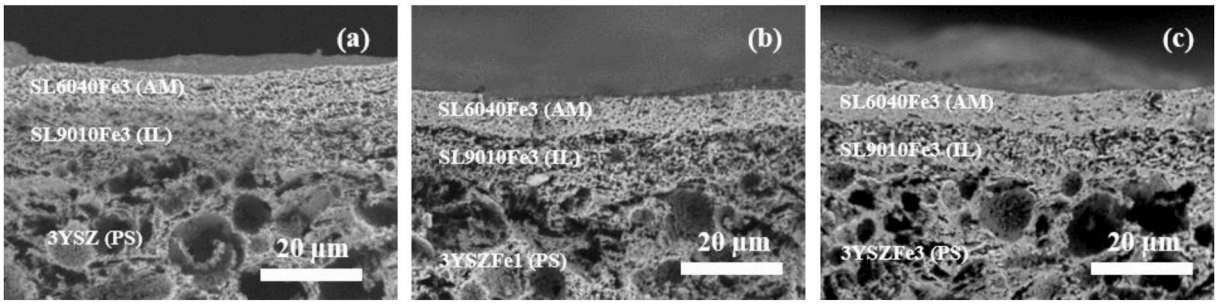


**Fig. 6.** Effect of the $Fe_2O_3$ content in the 3YSZ porous support (PS) on the densification of SL6040Fe3 active membranes (AM) after sintering at 1250 °C: a) 3YSZ porous support, b) 3YSZFe1 and c) 3YSZFe3. SL9010Fe3 was used as the inner activation layer (IL).

**Table 4**
EDS elemental composition of the two phases in the active membranes. Compositions are normalized to Zr for the ScYSZ and to La in the case of the LCCN.

| | ScYSZ, Zr = 0.89 | | | LCCN, La = 1 | | | |
|---|---|---|---|---|---|---|---|
| Element | Sc | Y | Fe | Cr | Cu | Ni | Fe |
| Theoretical | 0.20 | 0.02 | -/0.01/0.03 | 0.85 | 0.10 | 0.05 | - |
| SL7030 | 0.20 | 0.05 | 0.03 | 0.66 | 0.01 | 0.02 | 0.20 |
| SL7030Fe1 | 0.19 | 0.04 | 0.06 | 0.60 | 0.02 | 0.02 | 0.28 |
| SL7030Fe3 | 0.19 | 0.04 | 0.05 | 0.80 | 0.04 | 0.03 | 0.09 |

density was obtained with the fastest heating rate: 98% densification was achieved in SL7030Fe3 sintered at 1250 °C using a ramp of 200 °C $h^{-1}$, while 92% densification was obtained using 60 °C $h^{-1}$.

The effect of the heating rate can be explained with the results of our thermomechanical study (Section 3.1.1). The total shrinkages of SL7030Fe3 and 3YSZFe3 after sintering at 1250 °C are ~11% and ~18%, respectively, and from 950 °C to 1150 °C the 3YSZFe3 shrinks faster than the SL7030Fe3 (Fig. 3). This means that if the heating rate is slow, the 3YSZFe3 support has enough time to shrink already at low temperatures (below 1150 °C), where the SL7030Fe3 active membrane attached to the support is unable to shrink at the same rate. Reaching the sintering dwell temperature (1250 °C), the already sintered support cannot shrink much further, which places the active membrane under tensile stress while it is sintering. To release the tension, the membrane would crack in some areas and locally sinter and densify. When the heating rate is increased from 60 to 200 °C $h^{-1}$, the 3YSZFe3 support has less time to shrink at low temperatures, allowing the SL7030Fe3 membrane to shrink and densify together with the 3YSZFe3 support during the dwell time at 1250 °C.

The same positive effect of increased heating rate in the sintering cycle was also observed for the combination of the SL4060 active membrane and a 3YSZFe3 porous support (Fig. S1 in the supplementary information).

### 3.3.4. *Effect of the inner activation layer*

A porous layer was introduced between the porous support and the active membrane to (i) increase the quantity of triple phase boundaries (TPB) where the surface exchange reactions can take place and (ii) to improve the gas diffusion from the gas stream to the TPBs. ScYSZ has been used as an activation layer between the 3YSZ and ScYSZ-LCCN6040 in previous studies [29]. Since LCCN hinders the densification when added to ScYSZ, the possibility of using LCCN as a pore former in the activation layers was investigated. Consequently, LCCN was added not only to provide electronic conductivity, but also to utilize its low degree of densification to form a porous structure. Multilayer tubes were fabricated with SL9010Fe3, SL8020Fe3 or SL7030Fe3 as inner activation layers and SL6040Fe3 as active membrane on 3YSZFe3 porous supports.

The SEM images (Fig. 8) show how the LCCN content of the inner layer affects the densification of the SL6040Fe3 active membrane. Membrane densities of 95%, 90% and 70% were obtained for

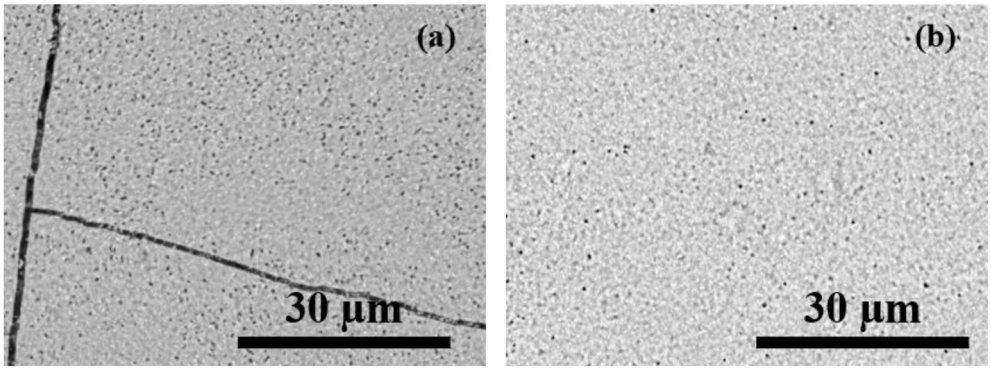


**Fig. 7.** SEM micrographs of the top-view of the SL7030Fe3 active membranes supported on 3YSZFe3 tubes sintered with two different heating rates: a) 60 °C $h^{-1}$, b) 200 °C $h^{-1}$.

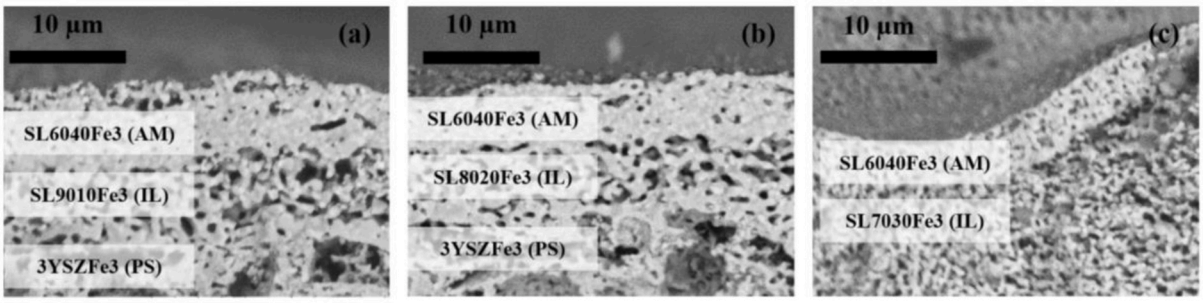


**Fig. 8.** SEM cross-section images of 3YSZFe3 porous supports (PS) and SL6040Fe3 active membranes (AM), with inner activation layers (IL) containing three different amounts of LCCN: a) SL9010Fe3, b) SL8020Fe3 and c) SL7030Fe3.

SL9010Fe3, SL8020Fe3 and SL7030Fe3, respectively. Using SL9010Fe3 allows forming TPB sites at the inner layer – active membrane interface, without limiting the densification of the active membrane, while a LCCN-content higher than 20 vol% leads to a too porous membrane layer, as observed in Fig. 8c. If no sintering aid was used in the inner activation layer, temperatures as high as 1100 °C would be required to bond it to the porous support. This would cause too much shrinkage of the porous support, such that it would not be able to co-sinter with the active membrane in the subsequent processing step.

### 3.3.5. *Outer activation layer*

As a last step to obtain a complete multi-layered membrane, it is necessary to deposit a porous outer activation layer to increase the TPB. The outer layer was deposited after sintering of the active membrane (Fig. 2), which allows using a low-density, high-LCCN content composites for the outer layer. Consequently, tubular, asymmetric OTM consisting of 3YSZFe3 - SL9010Fe3 - SL7030Fe3 (porous support - inner activation layer - active membrane) and SL7030Fe3, SL6040Fe3 or SL5050Fe3 as the outer activation layer were manufactured.

Only SL7030Fe3 attached to the active membrane at 1200 °C, while SL6040Fe3 and SL5050Fe3 did not properly attach even at 1250 °C. This is because larger quantities of LCCN decreases the sinterability of the LCCN-ScYSZ composite. Temperatures higher than 1300 °C would then be needed to properly adhere to the membrane, which would lead to formation of the insulating $LaZr_2O_7$ phase [29].

## 3.4. *Performance of optimized asymmetrical tubular oxygen membranes*

The possible porous support/active membrane combinations based on the thermochemical analysis (Section 3.2) are after the investigations reported in Section 3.3 reduced to those with 3YSZFe3 porous supports, SL9010Fe3 inner activation layers, and SL7030Fe3 outer activation layer. The content of dopant in the active membrane was not found to be critical. The performance of complete tubular, asymmetric OTM systems with different active membrane layers were therefore studied.

Fig. 9 shows cross-section SEM micrographs of an OTM containing SL7030Fe1 as the active membrane layer. An OTM containing SL7030Fe3 as active membrane showed the same microstructure; the densification of the active membrane layer was independent of the Fe content. The membranes were gas-tight and no delamination or cracks could be observed, which makes these configurations using SL7030 or SL7030Fe1 as the active membrane feasible options for further study and characterization. Tubes of 30 cm length could be fabricated and reproduced.

### 3.4.1. *Thermomechanical and chemical stability of the membranes*

Thanks to the optimization described in the previous sections, 30 cm long tubular asymmetric OTMs made of 3YSZFe3 porous support, SL9010Fe3 inner activation layer, SL7030Fe1 active membrane and SL7030Fe3 outer activation layer were successfully fabricated. The tubes were exposed to thermal cycling in air, reducing conditions and re-oxidation. The cross-sectional micrographs and the photograph of the tubes (Fig. 10) show that the membrane was crack-free, without macro- or micro-structural defects after each stage of the treatment. This indicates high mechanical stability of the porous support as well as strong interfaces between all layers. The support turned black after the reduction step, probably due to reduction of $Fe^{4+}$ to $Fe^{3+}$ [46].

The elemental composition from EDS analysis of the active membrane layer (SL7030Fe3) after sintering and after reduction are shown in Table 5. After sintering, the LCCN phase has lost ~50% of the Cu and 13% of the Cr relative to its nominal composition, but no further changes to the composition are observed after the reduction step.

### 3.4.2. *Oxygen permeation flux*

The optimized OTM (3YSZFe3 porous support, SL9010Fe3 inner activation layer, SL7030Fe1 active membrane and SL7030Fe3 outer activation layer) was characterized in terms of oxygen permeation flux on a ~3 cm tubular section. The test was performed from 850 °C to

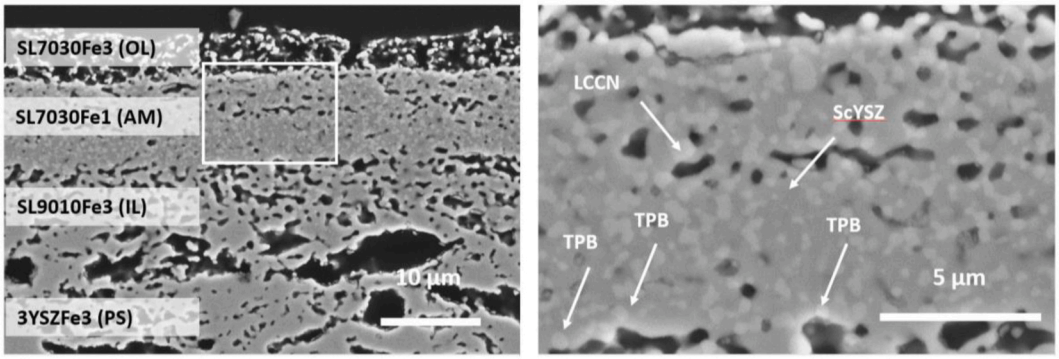


**Fig. 9.** SEM images of cross-sections of a) an OTM made of 3YSZFe3 (porous support), SL9010Fe3 (inner layer), SL7030Fe1 (active membrane) and SL7030Fe3 (outer layer); and b) zoomed-in view of the SL7030Fe1 (active membrane).

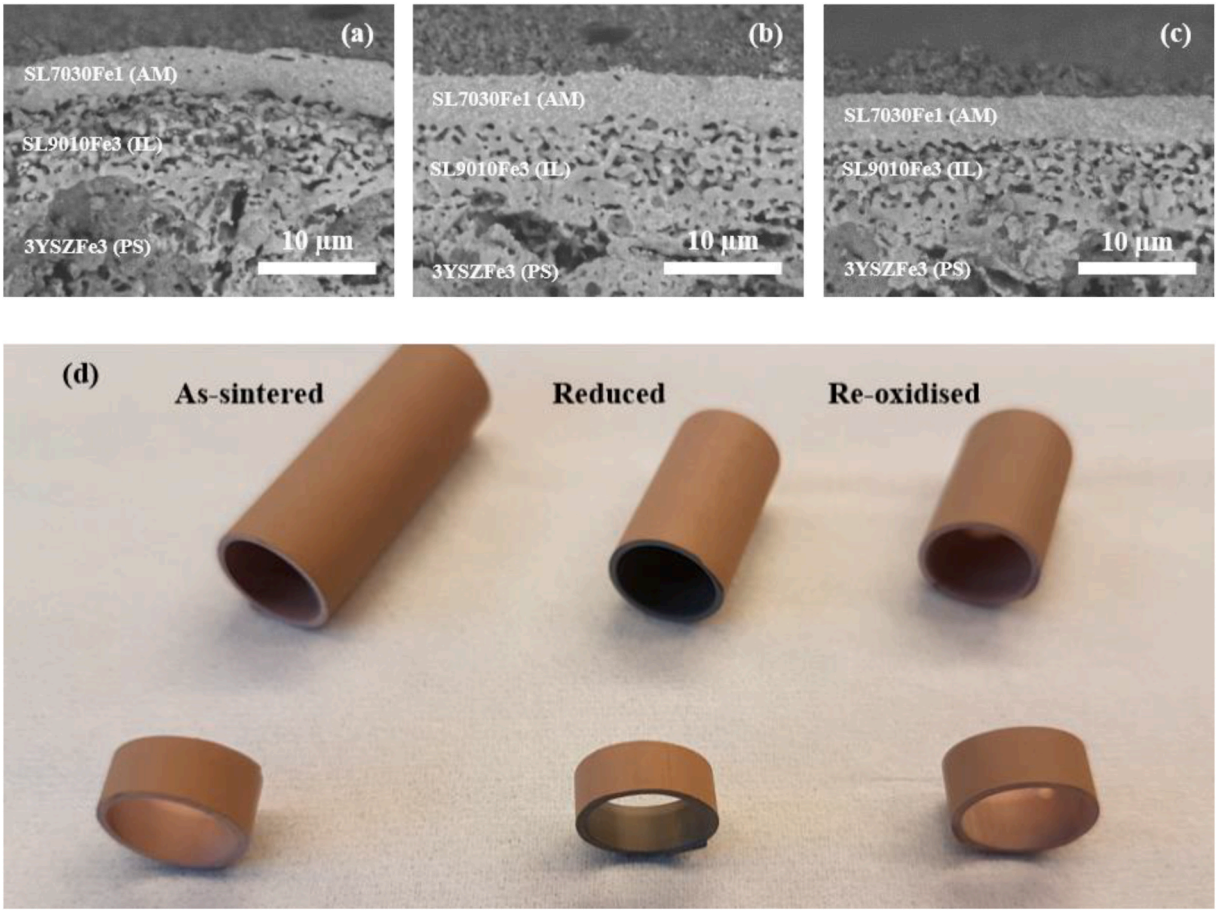


**Fig. 10.** SEM images of the cross-section of the tube after cyclic treatments at 1000 °C in a) air, b) 5%$H_2$–$N_2$ and c) re-oxidised sample. d) Photograph of the samples. The outer diameter of the tubes are 1 cm.

**Table 5**
EDS analysis of the SL7030Fe3 active membrane in different testing stages. Atomic values of the different components are normalized to Zr (for ScYSZ) and La (for LCCN).

| Element | Nominal | Sintered | Reduced |
|---|---|---|---|
| Zr | 0.89 | 0.89 | 0.89 |
| Y | 0.02 | 0.04 | 0.04 |
| Sc | 0.20 | 0.14 | 0.10 |
| La | 1.00 | 1.00 | 1.00 |
| Cr | 0.85 | 0.78 | 0.78 |
| Cu | 0.10 | 0.04 | 0.04 |
| Ni | 0.05 | 0.04 | 0.04 |

950 °C. Fig. 11a shows the results from measurements in an air/$N_2$ gradient. The maximum oxygen flux (0.28 Nml $cm^{-2}$ $s^{-1}$) is obtained at 950 °C with a sweep gas rate of 500 ml•$min^{-1}$. This flux value is slightly higher than the oxygen flux obtained in a 1 mm pellet of ScYSZ-LCCN with the same operating conditions [28], which is one order of magnitude lower than the oxygen flux expected for a ~10 µm thick membrane. Measurements were also performed with $CO_2$, 5%$H_2$–$N_2$ and $H_2$ as the sweep gas, but the oxygen flux data of these measurements could not be obtained due to a failure in the mass flow controllers that affected the continuous and correct supply of the sweep gases. However, after each measurement performed with different sweep gases the oxygen permeation flux was measured in air/$N_2$ at 850 °C (Fig. 11b) to check the membrane stability after the different operation conditions. The oxygen flux is relatively unchanged after the tests in air/$CO_2$ and air/5%$H_2$–$N_2$ gradients, indicating a high stability of the membrane materials. A slightly higher oxygen flux was observed after measurements in air/$H_2$, probably caused by activation of the membrane due to reduction of the activation layer. While these test were only running over a few hours, the same membrane composition in a planar configuration was, after a slight initial decay, stable in $CO_2$ for 250 h [47].

The performance of the OTM relies on both the ionic conductivity of the ScYSZ and the electronic conductivity of LCCN, which might be affected by doping. To the best of our knowledge, there are no studies of the effect of Fe on the electronic conductivity on LCCN. This could be determined by electronic conductivity tests in relevant conditions, as well as careful XRD analysis to identify any substitution of Fe in the LCCN crystal lattice.

On the other hand, several studies [48–53] have investigated the effect of $Fe_2O_3$ on the ionic conductivity of the YSZ and other $ZrO_2$-based oxides. Simulations carried out by Chen et al. showed that oxygen ion conductivity could increase from 0.08 S•$cm^{-1}$ to 0.3028 S $cm^{-1}$ at 700 °C when 3 mol% $Fe_2O_3$ was added to the 8YSZ [51]. Bohnke et al. determined experimentally that the bulk conductivity of scandia-stabilized zirconia is not affected by the addition of $Fe_2O_3$, keeping values close to $3 \times 10^{-3}$ S $cm^{-1}$ in air at 750 °C [49]. Van Hassel et al. [54] measured the ionic conductivity of an Fe-doped single crystal of $(ZrO_2)_{0.83}(Y_2O_3)_{0.17}$ as function of $pO_2$ ($H_2$ and $N_2$ atmospheres) and temperature (500 °C – 900 °C). At 500 °C, the ionic conductivity was found to be one order of magnitude lower than the one of the single crystal. This has been explained by the possible incorporation of $Fe^{3+}$ on a $Zr^{4+}$ lattice position in the YSZ lattice. Nevertheless, above 700 °C the ionic conductivities converge despite the used atmosphere. To the best of the authors' knowledge, no studies of conductivity of Fe-doped ScYSZ in reducing conditions have been done. However, it is expected that ScYSZ follows a similar behaviour as YSZ crystal structures. Thus, the

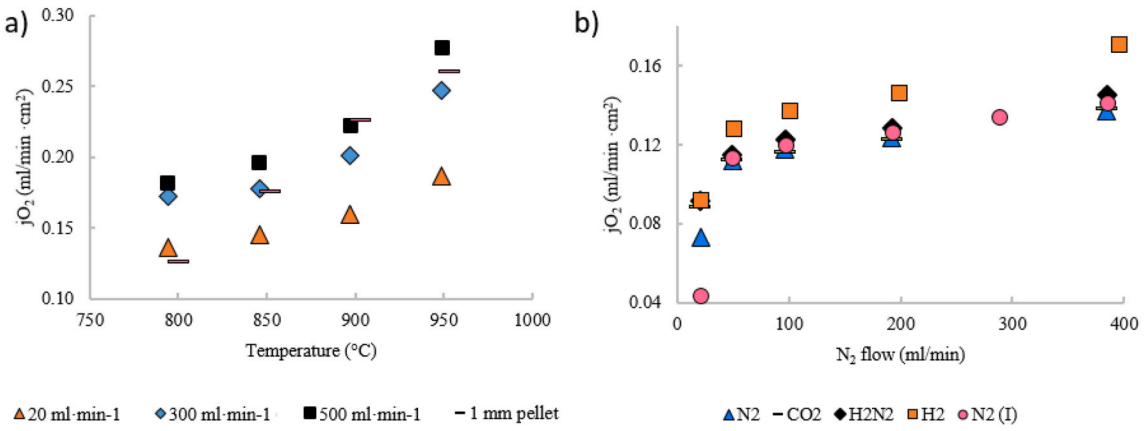


**Fig. 11.** Oxygen flux of tubular OTM based on SL7030Fe1 active membrane. a) Measurements in an air/$N_2$ gradient at different temperatures and flow rates b) Measurement in air/$N_2$ gradient after test with different sweep gasses. N2(I) refers to the $N_2$/air gradient measurement performed after all the tests with the different sweep gases.

ionic conductivity of the ScYSZ should not be compromised by the addition of $Fe_2O_3$ when working above 700 °C.

The lower oxygen flux values obtained when using sweep gas flows of 20 ml•$min^{-1}$ might be related to gas diffusion limitations. Other possible causes of the low oxygen permeability could be lack of electronic-conducting phase percolation and triple phase boundaries. This could be analyzed by means of 3D SEM and statistical 2D SEM studies. Any formation of $LaZr_2O_7$ insulating phase could be observable by transmission electron microscopy (TEM). Additional characterization of the fabricated membranes is therefore required to identify the reason (s) for the limited oxygen permeability. An extensive oxygen flux measurement campaign with relevant gases for syngas applications can also provide further insight. In addition, infiltration of a catalyst into the porous activation layers could help to overcome any surface exchange limitations to the oxygen flux. Still, the stable oxygen flux values after the using different gradients clearly indicates that the membrane has an outstanding stability towards different atmospheres, including highly reducing conditions, fulfilling one of the main requirements for syngas applications.

## 4. Conclusions

Tubular, asymmetric oxygen transport membranes with $(Sc_2O_3)_{0.10}(Y_2O_3)_{0.01}(ZrO_2)_{0.89}$ – $LaCr_{0.85}Cu_{0.10}Ni_{0.05}O_{3-\delta}$ (ScYSZ-LCCN) as the active membrane layer on $(Y_2O_3)_{0.03}(ZrO_2)_{0.97}$ (3YSZ) porous supports were successfully prepared by using $Fe_2O_3$ addition in the porous supports and in the dense dual-phase membrane layers. The addition of $Fe_2O_3$ increased the sintering activity of both materials and decreased mismatches observed between the layers in both thermal expansion coefficients and the sintering activity, which diminished the thermo-mechanical stresses. By the addition of $Fe_2O_3$ and its action as a sintering aid, the membranes could be sintered at 1250 °C rather than 1400 °C, significantly reducing the Cr-evaporation, which otherwise hinders full densification.

Specifically, adding 3 mol% $Fe_2O_3$ to the 3YSZ porous support lowered the onset of sintering by 80 °C, lead to an additional shrinkage of ~6% at 1250 °C and increased the strength of the tubes to >138 MPa without compromising the gas permeability. Only the active membranes co-sintered with the 3 mol% $Fe_2O_3$ doped 3YSZ porous support reached sufficient densification to be gas-tight, independently of the amount of $Fe_2O_3$ added to the active membrane layer. This demonstrates that the main factor that enables the densification of LCCN-based membrane layers is a good match of the shrinkage between the membrane layer and the support.

Dense membranes without cracks could be obtained after increasing the heating rate from 60 to 200 °C $h^{-1}$ in the temperature range 600–1250 °C. The shorter time spent below 1250 °C provided less time for the support to shrink before the membrane had reached its sintering onset temperature, and therefore reduced the sintering mismatches.

The ScYSZ inner and outer activation layers were successfully modified with LCCN to increase porosity and triple phase boundaries, and with $Fe_2O_3$ to decrease the sintering temperature.

We obtained an oxygen permeation flux of approximately 0.28 ml•$min^{-1}$•$cm^2$ in an air/$N_2$ gradient at 950 °C. A further increase in performance could possibly be achieved by improving the percolation of the electronic conducting phase, and enhancing the surface exchange. The manufactured tubular, asymmetric oxygen transport membrane showed high stability after exposure to $CO_2$ and reducing conditions and high mechanical stability towards cycling, making it a promising candidate for further investigation and application in syngas or oxy-fuel combustion.

## Declaration of interest

The authors declare that they have no known competing financial interests or personal relationships that could have appeared to influence the work reported in this paper.

## Acknowledgements

This research was partly funded by Energinet.dk through grant number 12403 “Highly Flexible Energy Production by Oxy-Fired Biomass Gasification” and partly by the FLEXSNG project. This project has received funding from the European Union’s Horizon 2020 research and innovation programme under grant agreement no. 101022432.

## Appendix A. Supplementary data

Supplementary data to this article can be found online at https://doi.org/10.1016/j.oceram.2022.100292.

## References

[1] J. Da Costa, S. Smart, J. Motuzas, L. Shaomin, D. Zhang, State of art (SOTA) report on dense ceramic membranes for oxygen separation from air, Aust. Natl. Low Emiss. Coal Res. Dev. (ANLEC R&D) (2013) 1–13 [Online]. Available: http://www.globalccsinstitute.com/publications/state-art-sota-report-dense-ceramic-membranes-oxygen-separation-air.

[2] M. Riaz, M. Abdullah Butt, Oxygen transport membranes and their role in $CO_2$ capture and syngas production, J. Membr. Sci. Technol. (2018), https://doi.org/10.4172/2155-9589.1000181, 08, no. 02.

[3] E. John, An A-Z Guide to the Elements, vol. 539, Oxford Univ. Press, 2001.

[4] T. Banaszkiewicz, M. Chorowski, W. Gizicki, Comparative analysis of cryogenic and PTSA technologies for systems of oxygen production, AIP Conf. Proc. 1573 (1) (Feb. 2015) 1373, https://doi.org/10.1063/1.4860866.

[5] Y. Wei, W. Yang, J. Caro, H. Wang, Dense ceramic oxygen permeable membranes and catalytic membrane reactors, Chem. Eng. J. 220 (Mar. 2013) 185–203, https://doi.org/10.1016/j.cej.2013.01.048.

[6] R. Kiebach, et al., A review on dual-phase oxygen transport membranes: from fundamentals to commercial deployment, J. Mater. Chem. 10 (5) (Feb. 2022) 2152–2195, https://doi.org/10.1039/D1TA07898D.

[7] A. Julbe, D. Farrusseng, C. Guizard, Limitations and potentials of oxygen transport dense and porous ceramic membranes for oxidation reactions, Catal. Today 104 (2–4) (Jun. 2005) 102–113, https://doi.org/10.1016/J.CATTOD.2005.03.075.

[8] M.J. Den Exter, W.G. Haije, J.F. Vente, Viability of ITM technology for oxygen production and oxidation processes: material, system, and process aspects, Inorg. Membr. Energy Environ. Appl. (2009) 27, https://doi.org/10.1007/978-0-387-34526-0_2. –51.

[9] M. Puig-Arnavat, et al., Integration of mixed conducting membranes in an oxygen–steam biomass gasification process, RSC Adv. 3 (43) (Oct. 2013) 20843, https://doi.org/10.1039/c3ra44509g.

[10] H. Stadler, et al., Oxyfuel coal combustion by efficient integration of oxygen transport membranes, Int. J. Greenh. Gas Control 5 (1) (2011) 7–15, https://doi.org/10.1016/j.ijggc.2010.03.004.

[11] J. Garcia-Fayos, V.B. Vert, M. Balaguer, C. Solís, C. Gaudillere, J.M. Serra, Oxygen transport membranes in a biomass/coal combined strategy for reducing $CO_2$ emissions: permeation study of selected membranes under different $CO_2$-rich atmospheres, Catal. Today 257 (2) (Nov. 2015) 221–228, https://doi.org/10.1016/J.CATTOD.2015.04.019.

[12] C. Niedrig, W. Menesklou, S.F. Wagner, E. Ivers-Tiffée, High-temperature $pO_2$ stability of metal oxides determined by amperometric oxygen titration, J. Electrochem. Soc. 160 (2) (Dec. 2013) F135–F140, https://doi.org/10.1149/2.063302JES/XML.

[13] J. Yi, M. Schroeder, High temperature degradation of $Ba_{0.5}Sr_{0.5}Co_{0.8}Fe_{0.2}O_{3-\delta}$ membranes in atmospheres containing concentrated carbon dioxide, J. Membr. Sci. 378 (1–2) (Aug. 2011) 163–170, https://doi.org/10.1016/J.MEMSCI.2011.04.044.

[14] A. Waindich, A. Möbius, M. Müller, Corrosion of $Ba_{1-x}Sr_xCo_{1-y}Fe_yO_{3-\delta}$ and $La_{0.3}Ba_{0.7}Co_{0.2}Fe_{0.8}O_{3-\delta}$ materials for oxygen separating membranes under Oxycoal conditions, J. Membr. Sci. 337 (1–2) (Jul. 2009) 182–187, https://doi.org/10.1016/J.MEMSCI.2009.03.041.

[15] M. Arnold, H. Wang, A. Feldhoff, Influence of $CO_2$ on the oxygen permeation performance and the microstructure of perovskite-type $(Ba_{0.5}Sr_{0.5})(Co_{0.8}Fe_{0.2})O_{3-\delta}$ membranes, J. Membr. Sci. 293 (1–2) (Apr. 2007) 44–52, https://doi.org/10.1016/J.MEMSCI.2007.01.032.

[16] X. Zhu, W. Yang, Critical Factors Affecting Oxygen Permeation through Dual-phase Membranes, first ed., vol. 14, Elsevier BV., 2011.

[17] M.M. Nasrallah, D.L. Douglass, Ionic and electronic conductivity in $Y_2O_3$-doped monoclinic $ZrO_2$, J. Electrochem. Soc. 121 (2) (1974) 255–262.

[18] T. Ishihara, Oxide ion-conducting materials for electrolytes, Mater. High-Temperature Fuel Cells (Jan. 2012) 97–132, https://doi.org/10.1002/9783527644261.CH3.

[19] H. Liu, S. Li, Q. Li, Y. Li, Investigation on the phase stability, sintering and thermal conductivity of $Sc_2O_3$–$Y_2O_3$–$ZrO_2$ for thermal barrier coating application, Mater. Des. 31 (6) (Jun. 2010) 2972–2977, https://doi.org/10.1016/J.MATDES.2009.12.019.

[20] V.G. Artemov, et al., Analysis of electric properties of $ZrO_2$-$Y_2O_3$ single crystals using teraherz IR and impedance spectroscopy techniques, Russ. J. Electrochem. 50 (7) (2014) 690–693, https://doi.org/10.1134/S1023193514070039.

[21] S. Gupta, M.K. Mahapatra, P. Singh, Lanthanum chromite based perovskites for oxygen transport membrane, Mater. Sci. Eng. R Rep. 90 (2015) 1–36, https://doi.org/10.1016/j.mser.2015.01.001.

[22] J.W. Fergus, Lanthanum chromite-based materials for solid oxide fuel cell interconnects, Solid State Ionics 171 (1–2) (Jun. 2004) 1–15, https://doi.org/10.1016/J.SSI.2004.04.010.

[23] A.C. Khandkar, C.E. Milliken, S. Elangovan, J.J. Hartvigsen, US5958304A - Doped Lanthanum Chromite Material for Bipolar Interconnects for Solid Oxide Fuel Cells, 1999.

[24] S. Gupta, P. Singh, Nickel and titanium doubly doped lanthanum strontium chromite for high temperature electrochemical devices, J. Power Sources 306 (Feb. 2016) 801–811, https://doi.org/10.1016/J.JPOWSOUR.2015.11.111.

[25] C. Sarno, I. Luisetto, F. Zurlo, S. Licoccia, E. Di Bartolomeo, Lanthanum chromite based composite anodes for dry reforming of methane, Int. J. Hydrogen Energy 43 (31) (Aug. 2018), 14742, https://doi.org/10.1016/J.IJHYDENE.2018.06.021, 14750.

[26] S. Tanasescu, A. Orasanu, D. Berger, I. Jitaru, J. Schoonman, Electrical conductivity and thermodynamic properties of some alkaline earth-doped lanthanum chromites, Int. J. Thermophys. 26 (2) (2005) 543–557, https://doi.org/10.1007/S10765-005-4516-7, 2005 262.

[27] Y. Orikasa, et al., Surface strontium segregation of solid oxide fuel cell cathodes proved by in situ depth-resolved x-ray absorption spectroscopy, ECS Electrochem. Lett. 3 (4) (Jan. 2014), https://doi.org/10.1149/2.006404EEL.

[28] S. Pirou, et al., Performance and stability of $(ZrO_2)_{0.89}(Y_2O_3)_{0.01}(Sc_2O_3)_{0.10}$-$LaCr_{0.85}Cu_{0.10}Ni_{0.05}O_{3-\Delta}$ oxygen transport membranes under conditions relevant for oxy-fuel combustion, J. Membr. Sci. 552 (January) (Apr. 2018) 115–123, https://doi.org/10.1016/j.memsci.2018.01.067.

[29] A.B. Haugen, et al., Exploring the processing of tubular chromite- and zirconia-based oxygen transport membranes, Ceramics 1 (1) (2018) 229–245, https://doi.org/10.3390/ceramics1020019.

[30] S.A. Suvorov, A.P. Shevchik, Chemical equilibria involving lanthanum chromite, Refract. Ind. Ceram. 45 (2) (Mar. 2004) 94–99, https://doi.org/10.1023/B:REFR.0000029615.98571.67.

[31] C. Zhang, Y. Huang, L. Zeng, Y. He, P. Yu, H. Luo, Effects of Bi substitution on the cobalt-free 60wt.% $Ce_{0.9}Pr_{0.1}O_{2-\delta}$-40wt.%$Pr_{0.6}Sr_{0.4}Fe_{1-x}Bi_xO_{3-\delta}$ oxygen transport membranes, Processes 9 (10) (Oct. 2021) 1767, https://doi.org/10.3390/PR9101767/S1.

[32] J. Feng, Y. Fan, H. Qi, N. Xu, Co-sintering synthesis of tubular bilayer α-alumina membrane, J. Membr. Sci. 288 (1–2) (Feb. 2007) 20–27, https://doi.org/10.1016/j.memsci.2006.09.034.

[33] A.J. Flegler, T.E. Burye, Q. Yang, J.D. Nicholas, Cubic yttria stabilized zirconia sintering additive impacts: a comparative study, PB, Ceram. Int. 10 (40) (Dec. 2014), 16323, https://doi.org/10.1016/J.CERAMINT.2014.07.071, 16335.

[34] F. Guo, P. Xiao, Effect of $Fe_2O_3$ doping on sintering of yttria-stabilized zirconia, J. Eur. Ceram. Soc. 16 (32) (Dec. 2012) 4157–4164, https://doi.org/10.1016/J.JEURCERAMSOC.2012.07.035.

[35] D.K. Ramachandran, K. Kwok, M. Søgaard, F. Clemens, A.J. Glasscock, A. Kaiser, The role of sacrificial fugitives in thermoplastic extrusion feedstocks on properties of MgO supports for oxygen transport membranes, J. Eur. Ceram. Soc. 35 (5) (May 2015) 1527–1537, https://doi.org/10.1016/j.jeurceramsoc.2014.11.014.

[36] D.K. Ramachandran, F. Clemens, A.J. Glasscock, M. Søgaard, A. Kaiser, Tailoring the microstructure of porous MgO supports for asymmetric oxygen separation membranes: optimization of thermoplastic feedstock systems, Ceram. Int. 40 (7) (Aug. 2014), 10465, https://doi.org/10.1016/j.ceramint.2014.03.017, 10473.

[37] D.K. Ramachandran, M. Søgaard, F. Clemens, J. Gurauskis, A. Kaiser, Fabrication and performance of a tubular ceria based oxygen transport membrane on a low cost MgO support, Separ. Purif. Technol. 147 (Jun. 2015) 422–430, https://doi.org/10.1016/j.seppur.2015.02.037.

[38] K. Kwok, L. Kiesel, H.L. Frandsen, M. Søgaard, P.V. Hendriksen, Strength characterization of tubular ceramic materials by flexure of semi-cylindrical specimens, J. Eur. Ceram. Soc. 34 (5) (May 2014) 1423–1432, https://doi.org/10.1016/J.JEURCERAMSOC.2013.12.005.

[39] A.B. Haugen, A. Geffroy, A. Kaiser, V. Gil, MgO as a non-pyrolyzable pore former in porous membrane supports, J. Eur. Ceram. Soc. 38 (2018) 3279–3285, https://doi.org/10.1016/j.jeurceramsoc.2018.02.039. February.

[40] H. Hayashi, T. Saitou, N. Maruyama, H. Inaba, K. Kawamura, M. Mori, Thermal expansion coefficient of yttria stabilized zirconia for various yttria contents, Solid State Ionics 176 (5–6) (Feb. 2005) 613–619, https://doi.org/10.1016/j.ssi.2004.08.021.

[41] W. Fan, et al., Improved properties of scandia and yttria co-doped zirconia as a potential thermal barrier material for high temperature applications, J. Eur. Ceram. Soc. 38 (13) (Oct. 2018) 4502–4511, https://doi.org/10.1016/J.JEURCERAMSOC.2018.06.002.

[42] Y.P. Fu, H.C. Wang, Structure, electrical, and thermal expansion properties of $(La_{0.8}Ca_{0.2})(Cr_{0.9-x}Co_{0.1}Ni_x)O_{3-d}$ interconnect materials for intermediate temperature solid oxide fuel cells, J. Mater. Res. 24 (5) (May 2009) 1748–1755, https://doi.org/10.1557/JMR.2009.0207.

[43] A.B. Haugen, J. Gurauskis, A. Kaiser, M. Søgaard, Graphite and PMMA as pore formers for thermoplastic extrusion of porous 3Y-TZP oxygen transport membrane supports, J. Eur. Ceram. Soc. 37 (3) (2017) 1039–1047, https://doi.org/10.1016/j.jeurceramsoc.2016.10.001.

[44] C.G. Schmidt, K.B. Andersen, Z. Fu, K.K. Hansen, A. Roosen, A. Kaiser, Effect of pore formers on properties of tape cast porous sheets for electrochemical flue gas purification, J. Eur. Ceram. Soc. 36 (2015) 645–653, https://doi.org/10.1016/j.jeurceramsoc.2015.09.030.

[45] A.V. Mikhailov, N.A. Gribchenkova, E.N. Kolosov, A.R. Kaul, A.S. Alikhanyan, Mass spectrometric investigation of vaporization in the $Bi_2O_3$-$Fe_2O_3$ system, Russ. J. Phys. Chem. A 85 (1) (Dec. 2010) 26–30, https://doi.org/10.1134/S0036024411010183, 2011 851.

[46] A. Pineau, N. Kanari, I. Gaballah, Kinetics of reduction of iron oxides by $H_2$: Part I: low temperature reduction of hematite, Thermochim. Acta 447 (1) (Aug. 2006) 89–100, https://doi.org/10.1016/J.TCA.2005.10.004.

[47] S. Pirou, et al., Performance and stability of $(ZrO_2)_{0.89}(Y_2O_3)_{0.01}(Sc_2O_3)_{0.10}$-$LaCr_{0.85}Cu_{0.10}Ni_{0.05}O_{3-\Delta}$ oxygen transport membranes under conditions relevant for oxy-fuel combustion, J. Membr. Sci. 552 (January) (2018) 115–123, https://doi.org/10.1016/j.memsci.2018.01.067.

[48] S. Molin, M. Gazda, P. Jasinski, Interaction of yttria stabilized zirconia electrolyte with $Fe_2O_3$ and $Cr_2O_3$, J. Power Sources 194 (1) (Oct. 2009) 20–24, https://doi.org/10.1016/J.JPOWSOUR.2009.01.031.

[49] O. Bohnke, V. Gunes, K.V. Kravchyk, A.G. Belous, O.Z. Yanchevskii, O.I. V'Yunov, Ionic and electronic conductivity of 3mol% $Fe_2O_3$-substituted cubic yttria-stabilized $ZrO_2$ (YSZ) and scandia-stabilized $ZrO_2$ (ScSZ), Solid State Ionics (262) (Sep. 2014) 517–521, https://doi.org/10.1016/J.SSI.2013.11.003. C.

[50] V.I. Barbashov, N.N. Belousov, Conductivity of $Fe_2O_3$-doped YSZ, Ionics 8 (20) (Aug. 2014) 1051–1053, https://doi.org/10.1007/S11581-013-1052-5.

[51] Y.H. Chan, H.Y. Lai, C.K. Chen, Enhancing oxygen iron conductivity of 8YSZ electrolytes in SOFC by doping with $Fe_2O_3$, Comput. Mater. Sci. 147 (May 2018) 1–6, https://doi.org/10.1016/J.COMMATSCI.2018.01.057.

[52] B. Johar, N.A. Zaili, Fe-doped 8YSZ at different composition for solid electrolyte in solid oxide fuel cell, MATEC Web Conf 78 (Oct. 2016), 01102, https://doi.org/10.1051/MATECCONF/20167801102.

[53] D. Lybye, M. Mogensen, Effect of Transition Metal Ions on the Conductivity and Stability of Stabilised Zirconia, Mar. 2008, pp. 67–78, https://doi.org/10.1002/9780470291337.CH7.

[54] B.A. van Hassel, A.J. Burggraaf, Effect of ion implantation doping on electrical properties of yttria-stabilized zirconia thin films, Solid State Ionics 57 (3–4) (1992) 193–201, https://doi.org/10.1016/0167-2738(92)90148-I.